Optimized magnetron sputtering process for the deposition of gadolinia doped ceria layers with controlled structural properties

Martin Mickan, Pierre Coddet, Julien Vulliet, Amael Caillard, Thierry Sauvage, Anne-Lise Thomann

Optimized magnetron sputtering process for the deposition of Gadolinia doped Ceria layers with controlled structural properties

Martin Mickan[a*], Pierre Coddet[b], Julien Vulliet[b], Amael Caillard[a], Thierry Sauvage[c], Anne-Lise Thomann[a]

[a] GREMI (Groupe de Recherches sur l'Energétique des Milieux Ionisés) – UMR7344 CNRS/Université d'Orléans, 14 rue d'Issoudun, 45067 Orléans, France

[b] CEA DAM, Le Ripault, F-37260 Monts, France

[c] CNRS, UPR3079 CEMHTI, 1D avenue de la Recherche Scientifique, 45071, Orléans Cedex 2, France

* Corresponding author: martin.mickan@univ-orleans.fr
Phone: +33 2 38 41 71 36
Fax: +33 2 38 41 71 54

Abstract

Gadolinia doped ceria (GDC) films have been deposited using reactive magnetron sputtering and the influence of the deposition parameters on the properties of the films has been investigated. The oxygen flow rate, the target-substrate distance and the radio frequency substrate bias have been varied and films were deposited with a relatively high power-normalized growth rate of 15-18 nm min^{-1} W^{-1} cm^2. Depending on the target-substrate distance and on the oxygen flow rate fully oxidized as-deposited films were obtained or substoichiometric films, which need to be oxidized by an ex-situ thermal annealing step. These two manufacturing routes (direct deposition of a fully oxidized compound or post-oxidation of a sub-stoichiometric oxide) lead to different preferential orientations ([200] or [111]) of the final oxide film. This is attributed to the oxygen/metal flux ratio, which is modified according to the experimental configuration and the process parameters. Furthermore, the substrate bias was found to further the [111] orientation and thus playing with this parameter allows a fine tuning of the preferential orientation.

Keywords: Reactive magnetron sputtering, Gadolinia doped ceria, Thin films

1. Introduction

Solid oxide fuel cells, which can be reversibly used for high temperature steam electrolysis, are subject to chemical reactions during operation that can degrade their performance and therefore limit their lifetime. Especially in devices made of yttria-stabilized zirconia (YSZ) electrolytes and $La_{1-x}Sr_xCo_{1-y}Fe_yO_{3-\delta}$ (LSCF) electrodes, the diffusion of Sr can lead to the formation of insulating $SrZrO_3$ [1,2]. Gadolinia doped ceria (GDC) thin films can be used in such devices as a Sr diffusion barrier in order to extend their lifetime [3,4].

GDC layers are classically prepared by ceramic techniques such as screen printing [5] or wet-chemical techniques such as spin coating [6]. However, the deposition of thin and dense layers is difficult with these techniques with typical thicknesses of a few micrometers [7]. Physical vapor deposition techniques such as pulsed laser deposition [8], electron beam evaporation [9] or magnetron sputtering can be used to produce high quality films with a controlled thickness (less than 1 μm). Among these techniques, magnetron sputtering offers the advantage of easy scalability to industrial processes. There are several reports of the deposition of GDC films using both radio frequency (RF) [10–19] and direct current (DC) [4,7,20–32] magnetron sputtering, as well as high power impulse magnetron sputtering (HiPIMS) [33,34]. The different methods have each their own advantages and drawbacks. One problem is the deposition rate. While high deposition rates can be generally achieved in DC or RF sputtering, HiPIMS (leading to dense layers) generally gives lower deposition rates. Another problem is the cost of the deposition equipment, which is the lowest for DC sputtering. For this work, we chose to use reactive pulsed DC sputtering, because it is a relatively low cost process, which can be tuned to obtain high deposition rates.

While many of the publications on sputtering of GDC focus on the properties of the deposited GDC films [10,11,14–17,19–22,26,29,31,32], in this work, we want to focus on the process itself and on the optimization of the deposition conditions in order to achieve dense, stoichiometric GDC films at a high growth rate. In addition, we studied the influence of the process parameters such as the target-substrate distance, the oxygen flow rate and the substrate bias on the crystallographic orientation of the films. We investigated two routes, one furthering the deposition of fully oxidized films and another including the deposition of substoichiometric films followed by an ex-situ thermal oxidation treatment.

2. Materials and methods

GDC films have been deposited by reactive sputter deposition in a 35 L vacuum chamber using a 4-inch $Ce_{0.8}Gd_{0.2}$ target clamped on a balanced magnetron. A schematic of the chamber is shown in Figure 1. The target is powered in pulsed regime *pDC* (frequency of 50 kHz and an off-time of 5µs) using an Advanced Energy Pinnacle+ power supply regulated with a constant current (mean current of 1 A). Depending on the operating parameters (such as the oxygen flow rate), the mean voltage varies between 125 and 230 V, leading to a power range of 125-230 W.

The gas flow rate was fixed using Bronkhorst EL-FLOW mass flow controllers. The Ar flow rate was set to 20 sccm and the total pressure in the chamber was adjusted to 1 Pa using a gate valve before turning on the discharge. For one experiment, a higher Ar flow rate of 80 sccm was used in order to assess the influence of the pumping speed on the reactive sputter process. The pressure was measured using a capacitive gauge (Pfeiffer CCR375). A rotating substrate holder was used, which held pieces of [100] oriented P-doped Si wafers. The distance between the substrate and the target was fixed at 12.7 or 16.0 cm as shown in Figure 1. For some deposits, an RF bias of -40 to -80 V was applied on the substrate using an Advanced Energy Cesar 136 RF power supply corresponding to a delivered power of 4-9W and a reflected power of less than 1W. The deposition time for most of the samples was 15 min, leading to a film thickness of 600-700 nm. The influence of the gas inlet position was studied at two different locations (see gas inlet position 1 and 2 in Figure 1).

The deposition of the films took place in the metallic mode to achieve a high deposition rate of about 40 nm min^{-1}. In order to fully oxidize the films, in some cases a heat treatment after the deposition is necessary. This heat treatment was performed in air in a furnace (Nabertherm model LT5/13/B180) at 500°C with a heating rate 1°C/min and maintained at the maximum temperature for 1min as described in a previous work [7].

The chemical composition of the deposited layers was analyzed using Rutherford backscattering spectrometry (RBS) with a 2 MeV He ion beam in a Pelletron accelerator at the CEMHTI laboratory, Orleans (scattering angle of 165°). The experimental data were plotted using the software RUMP [35] and RBS spectra were fitted with simulated data in order to calculate the chemical composition. The morphology of the deposited films was investigated using a scanning

electron microscope (Carl Zeiss SMT, Supra-40, FEG-SEM). Additionally, energy dispersive X-ray spectroscopy (EDX, Bruker XFlash Detector 4010) was used to investigate the composition of the films. For the investigation of the crystalline properties, symmetrical θ/2θ scans were performed using a Bruker D8 Discover X-ray diffractometer in the parallel beam geometry with a Cu anode (Cu Kα line).

3. Results

In order to define the process parameters, the reactive sputtering of the CeGd target was investigated by following the target voltage evolution with respect to the oxygen flow rate between 0 and 6 sccm with a waiting time of 2 min between each point. Figure 2(a) shows the typical evolution of the discharge voltage for a pumping speed of 34 L s^{-1} (Ar flow rate of 20 sccm), while the corresponding evolution of the pressure is shown in Figure2(b). When the oxygen flow rate is increased, the discharge voltage stays at a high value of around 220 V at first. This is the metallic mode of the reactive sputtering process in which the target surface is in a metallic state and the oxygen is consumed by the growing film. Above a critical point at 2.5 sccm the discharge voltage decreases sharply (transition mode) to reach a lower level of 130-160V. As this low level is reached, the process is in the oxide mode, where the target is covered by an oxide layer. When decreasing the oxygen flow rate, the process encounters a transition back to the metallic mode, and a hysteresis behavior is observed. However, the discharge voltage does not directly return to its initial value. Instead, the target needs to be sputtered in a pure Ar atmosphere for more than 60 min as was observed in previous work [7]. The same behavior can also be seen in the pressure curve, but less pronounced. This problem may be related to the high reactivity of Ce and Gd towards oxygen. Ershov et al. [36] also observed that the voltage does not return to the initial value after a hysteresis experiment. In other publications, the voltage does return to its initial value as soon as 0 sccm oxygen is reached [30,37]. This may be related to the relatively high pumping speed used in these works, i.e. 236 L s^{-1} [30] or 109 L s^{-1} [37]. In order to test this hypothesis, we performed a hysteresis experiment at an Ar flow rate of 80 sccm and adjusted the pumping speed to 135 L s^{-1}, in order to keep the pressure (before adding oxygen) at 1 Pa. The resulting voltage and pressure curves are also shown in Figure 2. The lower slope in the pressure curve is due to the higher pumping speed. In this case, the critical point is shifted to a higher oxygen flow rate of 4.5 sccm.

When decreasing the oxygen flow rate, the voltage starts already to increase at an oxygen flow rate of 1.5 sccm. The initial value of the discharge voltage is reached after sputtering in pure Ar for 8 minutes. At high pumping speed the residence time of oxygen species close to the target is low, hindering the poisoning of the target and therefore limiting the growth of an oxide layer on the target. Thus, a high pumping speed allows the target to return to its initial state more easily. However, in order to avoid overheating of the pump and excessive Ar consumption, all other experiments in the present work were performed with a pumping speed of 34 L s^{-1}. Thus, particular care had to be taken in order to avoid entering the oxide mode, in order to impede target poisoning.

In follow-up experiments, the oxygen flow rate was increased up to 4 sccm with the same increasing rate (0.5 sccm/2 min) and then kept at this fixed value during a time where the target was sputtered in the oxide mode. After this time (varying between 2 and 80 min), the oxygen flow rate is set to 0 sccm. The time that was needed for the voltage to return to its initial value (230 V) was measured from that moment. Figure 3(a) displays the evolution of the voltage during the ramp of increasing oxygen flow rate, during the time where the O_2 is fixed to 4 sccm and during the time the voltage progressively increases without the presence of O_2. Figure 3(b) shows that the time needed to return to the metallic mode increased with the time that the target was sputtered in the oxide mode. This suggests that the oxide layer continues to grow during the sputtering process in the oxide mode. This is an evidence of the high reactivity of Ce and Gd towards oxygen. Due to this property, the oxygen poisoning of the target surface is difficult to remove, especially when the metal surface is exposed to oxygen during a long period. It should also be noted that the target voltage in the oxide mode keeps increasing, even though the oxygen flow rate is kept constant, as can be seen in Figure 3(a). This is another hint that the target oxidation process does not reach a steady state in the oxide mode and could be related to the continued increase of the oxide layer thickness during sputtering.

In order to avoid excessive consumption of target material, further experiments were stopped (oxygen flow rate set to 0 sccm) as soon as the critical point was surpassed and the target could return to the metallic mode in less than 10 min. The evolution of discharge voltage and pressure was recorded by increasing the oxygen flow rate by 0.5 sccm steps with a waiting time of 2 min at each step, while operating the discharge with a constant current of 1 A. This is shown in Figure 4 for two different target-substrate distances (12.7 and 16.0 cm). For the gas inlet position 1 (Figure

4(a)), the critical point was shifted from 3 sccm at the shorter distance to 4 sccm at the longer distance.

In order to investigate the reason for the shift in the critical point of the transition, the gas inlet position 2 was tested (close to the bottom of the vacuum chamber below the magnetron as shown in Figure 1). The experiments were repeated for both target-substrate distances as plotted in Figure 4(b). In this case, the critical point was found at the same flowrate of 3 sccm for both target-substrate distances. This suggests that placing the gas inlet close to the bottom of the chamber (position 2) leads to a higher localized oxygen concentration at the target, whereas placing the gas inlet between the target and substrate induces a higher localized oxygen concentration close to the substrate and the chamber walls in front of the target. These areas are submitted to the sputtered atom flux and thus are coated by a thin metallic film sensitive to oxidation. As the target-substrate distance increases, a larger part of the sputtered atoms is deposited on the chamber walls meaning on a larger surface. This leads to an increased global consumption of oxygen, so a higher oxygen flow rate is necessary to reach the transition from metallic to oxide mode. This behavior is thus explained by the change in the relative consumption of oxygen at the substrate and the chamber walls, and at the target.

An oxygen flow rate close to the critical point was chosen for the deposition of GDC films, to further the incorporation of oxygen inside the film during the deposition, while keeping the deposition rate high and avoiding target poisoning [7]. The gas was introduced at inlet position 1, in order to be able to use higher oxygen flow rates at a larger target-substrate distance. For target-substrate distances of 12.7 and 16.0 cm, the oxygen flow rate was set to 2 and 3 sccm, respectively. In both cases, the target voltage is equal to 230 V which means an average power of 230 W applied on this 4-inch target (specific power density of 2.8 W cm^{-2}).

First, the chemical composition of the films was investigated. EDX spectra were measured on a thick (>1µm) GDC film, to verify the Ce/Gd ratio. These results show, that the films contain a Ce/Gd ratio of 80%/20%, the same as the target. In order to evaluate the oxygen content of the films, RBS spectra were recorded on several deposited films, shown in Figure 5. The black line shows the fitted simulation that was obtained using the software RUMP. The fitted parameters include the concentration x of oxygen in $Ce_{0.8}Gd_{0.2}O_x$, the thickness of the films and a roughness factor (corresponding to the average thickness deviation expressed in 10^{15} at/cm^2) to take the surface roughness into account. The Ce/Gd ratio was fixed to 80%/20%, as confirmed by the EDX

analysis. After deposition at the shortest target-substrate distance, the films are not fully oxidized as evidenced by the RBS spectra shown in Figure 5(a, b, c). The as-deposited films can be fitted by a model using a thin layer at the extreme surface that exhibits an oxygen concentration gradient and a thicker sublayer that has a constant oxygen concentration corresponding to $Ce_{0.8}Gd_{0.2}O_{1.0}$ (floating and -40 V) or $Ce_{0.8}Gd_{0.2}O_{0.9}$ (-80 V). Only in two cases (Figure 5(a) and (c) corresponding to thin films deposited at short distance and with a floating / - 80 V biased substrate), the experimental data is not well fitted by the model at the interface between the layer and the substrate. The presence of the thin top layer with an oxygen gradient at the extreme surface can be explained by the incorporation of oxygen inside the films when the samples are exposed to air. This confirms that the as deposited films obtained at low substrate/target distance are not saturated in oxygen and remain sensitive to oxidation. After the annealing, the spectra can be fitted by the RUMP model containing a single layer of $Ce_{0.8}Gd_{0.2}O_2$, corresponding to a fully oxidized film. In case of the deposition at the longer target-substrate distance, the films are already fully oxidized in the as-deposited state, no thin top layer with oxygen gradient is visible and there is no difference before and after annealing in the RBS spectra shown in Figure 5(d, e, f). This confirms that a longer target-substrate distance (and therefore a change in the distance between the substrate and the gas inlet) can lead to an increased consumption of oxygen at the substrate as suggested by the transition shift shown in Figure 4.

The results of the fitting procedure are summarized in Table I. The thickness values correspond to the atom density (Ce, Gd and O) in the whole GDC layer and the thickness indicated in parentheses corresponds to the atom density of the oxygen-rich top thin film at the extreme surface. For films deposited at the same distance, the number of atoms is the same within an error margin of 10%. This number is decreased in the case of the films deposited at short distance before the annealing, which was expected considering that these films contain less oxygen. The thickness of the top layer obtained at short distance containing the oxygen gradient decreases with the substrate bias, as can be also seen in Figure 5(a, b, c). This suggests that the substrate bias might lead to the formation of a denser film that would allow less oxygen diffusion inside the sub-stoichiometric film when exposed to air. This cannot be observed on the films deposited at long distance, since they are fully oxidized before air exposure (absence of gradient top layer). The roughness was similar for the samples deposited at short distance, whereas for the films deposited at longer distance, the roughness parameter is decreasing with the substrate bias. In most cases, the annealing leads to an increase of the film roughness. This effect is especially pronounced for the films deposited at short

distance for which the oxygen content increased during this annealing, suggesting that roughness is related to volume expansion as the crystalline structure turns from a disordered metallic phase to oxide one. This is a well-known effect and is one of the causes of delamination when metal films are annealed in air [7].

Figure 6 shows X-ray diffractograms of the as-deposited films for the two different target-substrate distances in the 2θ range from 20 to 60°. For the films deposited at the shortest target-substrate distance, several overlapping peaks are visible that can be attributed to a phase mixture of Ce, Ce_7O_{12} and GDC. For the films deposited at the longest target-substrate distance, only peaks corresponding to GDC are visible. This confirms the RBS results: at the shortest distance, the films are substoichiometric in the as-deposited state, whereas for the longest distance, the films are fully oxidized. It should be noted, however, that for the films deposited at a longer target-substrate distance, the position of the peaks corresponding to GDC is slightly shifted to smaller values as compared to the reference positions. An elongation of the lattice parameter in the out-of-plane direction can indicate the presence of an in-plane compressive stress, which is often found in magnetron sputtered thin films due to bombardment of the growing film with energetic particles [38].

Figure 7 shows the X-ray diffractograms of the films after annealing at 500°C for the two different target-substrate distances in the 2θ range from 20 to 60°. For both distances and whatever the substrate bias, only peaks corresponding to GDC are visible. In this range, GDC has several peaks corresponding to the (111), (200), (220), (311) and (222) family of planes [39]. The positions of the peaks are close to the reference positions from the PDF card, indicating that the compressive in-plane stress could be relieved by the annealing procedure.

The XRD peaks in Figure 7 could be fitted with a Voigt function using the software Fityk [40]. From the integral intensity I of the peaks in the X-ray diffractograms the texture factor of the different crystallographic orientations can be calculated by taking into account the relative intensities I^{ref} of the peaks in case of a powder sample. The texture factor T_h for the lattice plane h can be calculated according to

$$T_h = \frac{I_h^{\mathrm{m}}/A_{\theta/2\theta}(\theta_h)}{I_h^{\mathrm{ref}}} \Big/ \sum \frac{I_{h'}^{\mathrm{m}}/A_{\theta/2\theta}(\theta_{h'})}{I_{h'}^{\mathrm{ref}}},$$

with I^{m} the measured intensity, I^{ref} the reference intensity and $\sum_h$, standing for the sum over all the diffraction peaks [41]. The reference intensities of the (111), (200), (220) and (311) diffraction peaks are taken from the JCPDS card 01-075-0162. The absorption factor $A_{\theta/2\theta}$ can be calculated by

$$A_{\theta/2\theta} = \left(1 - \exp\left(-\frac{2\mu t}{\sin\theta}\right)\right),$$

with t the film thickness and μ the linear attenuation coefficient [42]. The linear attenuation coefficient can be calculated with the software xraylib using the chemical composition and the theoretical density of GDC [43]. Considering that 4 different peaks are taken into account, using this definition of the texture factor means, that a completely random orientation would lead to a texture factor of 0.25 for each orientation, whereas a texture factor of 1 for a single orientation would describe a film fully oriented along that direction. Figure 8 shows the resulting texture factors. The films deposited at the shortest target-substrate distance show a random orientation without substrate bias and an increasingly preferential [111] orientation with increasing absolute value of the substrate bias. The films deposited at a longer target-substrate distance show a strong preferential [200] orientation without substrate bias that decreases with increasing the substrate bias (in absolute value).

Cross-sectional SEM micrographs of the films were observed before and after annealing and are shown in Figure 9. The images show that the as-deposited films have a columnar microstructure. For the films deposited at a distance of 12.7 cm, the columnar character of the microstructure of the films is less visible after the annealing, leading to a denser microstructure. The increase of the density can be explained by the volume expansion of the sub-stoichiometric films due to the oxidation during the annealing [44,45]. For the films deposited at a distance of 16.0 cm, the microstructure does not change during the annealing and remains columnar. This result is not surprising since these films do not exhibit a change of the composition after annealing, so there is no volume expansion.

The thickness of the films is about 750 nm (630 nm) for a target-substrate distance of 12.7 cm (16.0 cm), leading to a deposition rate of 50 nm $\mathrm{min^{-1}}$ (42 nm $\mathrm{min^{-1}}$). Taking into account the target power density of 2.8 W $\mathrm{cm^{-2}}$, this leads to a power-normalized deposition rate of 18 nm $\mathrm{min^{-1}}$ $\mathrm{W^{-1}}$ $\mathrm{cm^2}$ (15 nm $\mathrm{min^{-1}}$ $\mathrm{W^{-1}}$ $\mathrm{cm^2}$). Typical power-normalized deposition rates in the

literature for the deposition of GDC films using magnetron sputtering vary from less than 1 nm min^{-1} W^{-1} cm^2 [11,16,46] to around 2-8 nm min^{-1} W^{-1} cm^2 [3,28,30,33,34] as shown in Table II. Only a few works [12,19] report power-normalized deposition rates of more than 10 nm min^{-1} W^{-1} cm^2 using RF sputtering, which requires more expensive deposition equipment. The high power-normalized deposition rate in this work could be explained by the fact that the deposition takes place in the metallic mode.

4. Discussion

Both RBS as well as XRD results confirm that the films deposited at a longer target-substrate distance show an enhanced oxidation state as compared to films deposited at a shorter distance. This result can be explained by the observed shift of the transition. The shift of the critical point towards higher oxygen flow rates at the longest target-substrate distance allowed to use a higher oxygen flow rate while staying in the metallic mode. The higher oxygen flow rate of 3 sccm instead of 2 sccm led to an increase in the flux of oxygen towards the substrate in this case. At the same time, the flux of sputtered metal atoms towards the substrate decreases with increasing target-substrate distance. So, at the longest target-substrate distance the oxygen/metal flux ratio is expected to be high which is favorable to the growth of fully oxidized films, whereas at the shortest target-substrate distance the ratio of oxygen over metal flux at the substrate is low, leading to the growth of substoichiometric films.

The difference in the growth mechanism of the films at the two different target-substrate distances can also explain the different preferential orientations. In the works reported on the sputter deposition of GDC, only few papers report information about the crystalline orientation of the deposited films. Most of them indicate a random orientation [3,4,11,12,14,17–21,29,46] and only a few report a preferential [111] orientation [10,13,26,30,34]. The change from random to [111] orientation for the films deposited at the shortest distance in our work is in agreement with these works. In our case, a polycrystalline thin film consisting of a mixture of metallic and various substoichiometric phases with random orientation was oxidized to form a GDC film with mostly random orientation at the shortest target-substrate distance. With increasing substrate bias, positive ions can be accelerated towards the substrate, increasing their energy, which could suggest an

increase in the energy per arriving atom. A high energy per arriving atom could favor the growth along the [111] orientation, as the (111) surfaces have the lowest surface energy in fcc metals such as Ce [47].

On the other hand, at the longest target-substrate distance, the oxygen flow rate was higher and an oxide layer grew directly onto the substrates with a preferential [200] orientation. A preferential [200] orientation was not previously reported for sputter deposited GDC films except for epitaxial films deposited at high temperature on MgO substrates [13]. However, it was found by Van Steenberge et al. [37] for the deposition of pure CeO_2 films at oxygen flow rates close to the critical point. They explained the preferential [200] orientation by the suppression of the [111] orientation due to preferential sputtering of [111] oriented crystallites (planes with the highest surface atom density) by negative oxygen ion bombardment of the growing film [48]. If such a negative oxygen ion bombardment is also causing the [200] orientation in our case, it could also explain why the preferential orientation is less pronounced with increasing substrate bias, as the negative substrate bias would slow down the negative oxygen ions coming from the target leading to a more random orientation.

It is difficult from the features evidenced in this work to predict which GDC films will be the most efficient as diffusion barrier in electrochemical cells. A fully oxidized and crystallized compound is required to ensure a good ionic conductivity and a dense structure to avoid atomic diffusion. Working at longer distance allows synthesizing fully oxidized films in a single step, but leads to a columnar structure. In the second processing route investigated in the present work an annealing step is required to complete the oxidation state of the compound that has the advantage to densify the films by volume expansion (disappearance of the columnar structure). Electrochemical tests are underway to validate one or the other route. They will also allow to check whether the preferential orientation has a key influence on the performance in the application of solid oxide fuel cells, as it is known that the preferential orientation of thin films can have a large influence on performance and reliability in the case of other applications such as in microelectronics [49].

5. Conclusion

The deposition of thin GDC films on Si substrates by reactive pulsed DC magnetron sputtering with a high growth rate has been shown (18 $nm\,min^{-1}\,W^{-1}\,cm^2$). Mainly, two different growth conditions have been identified, that differ in their oxygen/metal flux ratio. A low oxygen/metal flux ratio leads to the deposition of substoichiometric films that need to be fully oxidized by an annealing post-treatment and show a stronger [111] orientation with increasing substrate bias. A high oxygen/metal flux ratio leads to the deposition of fully oxidized GDC films with a preferential [200] orientation that decreases with increasing substrate bias.

In a wider perspective, our study shows the ability to control the preferential orientation as well as the stoichiometry of magnetron sputtered oxide films by simply varying the process parameters and choosing a proper experimental configuration, which is less conventional. Here the oxygen flow rate, the gas inlet location and the target-substrate distance were found to play a great role on the deposition process and the final film properties. A finer control of the preferential orientation is even possible with RF substrate bias, suggesting the possibility to control the energy of the different ions arriving at the substrate.

Acknowledgements

The authors would like to thank Thomas Lecas and Hélène Lecocq for the technical support and the CERTeM for the funding for the SEM and XRD. This work was supported by the Region Centre Val de Loire in the Hytempe project in the framework of the Lavoisier program and the European Union through the European Regional Development Fund.

References

[1] H.Y. Tu, Y. Takeda, N. Imanishi, O. Yamamoto, Ln0.4Sr0.6Co0.8Fe0.2O3−δ (Ln=La, Pr, Nd, Sm, Gd) for the electrode in solid oxide fuel cells, Solid State Ion. 117 (1999) 277–281. https://doi.org/10.1016/S0167-2738(98)00428-7.

[2] M. Sase, D. Ueno, K. Yashiro, A. Kaimai, T. Kawada, J. Mizusaki, Interfacial reaction and electrochemical properties of dense (La,Sr) CoO3−δ cathode on YSZ (1 0 0), J. Phys. Chem. Solids. 66 (2005) 343–348. https://doi.org/10.1016/j.jpcs.2004.06.057.

[3] S. Uhlenbruck, N. Jordan, D. Sebold, H.P. Buchkremer, V.A.C. Haanappel, D. Stöver, Thin film coating technologies of (Ce,Gd)O2-δ interlayers for application in ceramic high-temperature fuel cells, Thin Solid Films. 515 (2007) 4053–4060. https://doi.org/10.1016/j.tsf.2006.10.127.

[4] S. Sønderby, T. Klemensø, B.H. Christensen, K.P. Almtoft, J. Lu, L.P. Nielsen, P. Eklund, Magnetron sputtered gadolinia-doped ceria diffusion barriers for metal-supported solid oxide fuel cells, J. Power Sources. 267 (2014) 452–458. https://doi.org/10.1016/j.jpowsour.2014.05.101.

[5] F.P.V. Berkel, Y. Zhang-Steenwinkel, G. Schoemakers, M.V. Tuel, B.G. Rietveld, Enhanced ASC Performance at 600°C by Ceria Barrier Layer Optimisation, ECS Trans. 25 (2009) 2717–2726. https://doi.org/10.1149/1.3205832.

[6] P. Plonczak, M. Joost, J. Hjelm, M. Søgaard, M. Lundberg, P.V. Hendriksen, A high performance ceria based interdiffusion barrier layer prepared by spin-coating, J. Power Sources. 196 (2011) 1156–1162. https://doi.org/10.1016/j.jpowsour.2010.08.108.

[7] P. Coddet, J. Vulliet, C. Richard, A. Caillard, A.-L. Thomann, Characteristics and properties of a magnetron sputtered gadolinia-doped ceria barrier layer for solid oxide electrochemical cells, Surf. Coat. Technol. 339 (2018) 57–64. https://doi.org/10.1016/j.surfcoat.2018.01.079.

[8] R. Knibbe, J. Hjelm, M. Menon, N. Pryds, M. Søgaard, H.J. Wang, K. Neufeld, Cathode–Electrolyte Interfaces with CGO Barrier Layers in SOFC, J. Am. Ceram. Soc. 93 (2010) 2877–2883. https://doi.org/10.1111/j.1551-2916.2010.03763.x.

[9] Y.S. Hong, S.H. Kim, W.J. Kim, H.H. Yoon, Fabrication and characterization GDC electrolyte thin films by e-beam technique for IT-SOFC, Curr. Appl. Phys. 11 (2011) S163–S168. https://doi.org/10.1016/j.cap.2011.03.071.

[10] Y.-L. Kuo, C. Lee, Y.-S. Chen, H. Liang, Gadolinia-doped ceria films deposited by RF reactive magnetron sputtering, Solid State Ion. 180 (2009) 1421–1428. https://doi.org/10.1016/j.ssi.2009.08.016.

[11] S.-E. Lin, Y.-L. Kuo, C.-H. Chou, W.-C.J. Wei, Characterization of electrolyte films deposited by using RF magnetron sputtering a 20mol% gadolinia-doped ceria target, Thin Solid Films. 518 (2010) 7229–7232. https://doi.org/10.1016/j.tsf.2010.04.082.

[12] Y.-L. Kuo, Y.-S. Chen, C. Lee, Growth of 20mol% Gd-doped ceria thin films by RF reactive sputtering: The O2/Ar flow ratio effect, J. Eur. Ceram. Soc. 31 (2011) 3127–3135. https://doi.org/10.1016/j.jeurceramsoc.2011.05.002.

[13] J. Jiang, W. Shen, J.L. Hertz, Fabrication of epitaxial zirconia and ceria thin films with arbitrary dopant and host atom composition, Thin Solid Films. 522 (2012) 66–70. https://doi.org/10.1016/j.tsf.2012.09.013.

[14] W. Wu, X. Wang, Z. Liu, Z. Zhao, D. Ou, B. Tu, M. Cheng, Influence of Deposition Temperature of GDC Interlayer Deposited by RF Magnetron Sputtering on Anode-Supported SOFC, Fuel Cells. 14 (2014) 171–176. https://doi.org/10.1002/fuce.201300158.

[15] T. Park, Y.H. Lee, G.Y. Cho, S. Ji, J. Park, I. Chang, S.W. Cha, Effect of the thickness of sputtered gadolinia-doped ceria as a cathodic interlayer in solid oxide fuel cells, Thin Solid Films. 584 (2015) 120–124. https://doi.org/10.1016/j.tsf.2015.03.010.

[16] J. Bae, D. Lee, S. Hong, H. Yang, Y.-B. Kim, Three-dimensional hexagonal GDC interlayer for area enhancement of low-temperature solid oxide fuel cells, Surf. Coat. Technol. 279 (2015) 54–59. https://doi.org/10.1016/j.surfcoat.2015.07.066.
[17] Y.-L. Kuo, S.-E. Lin, W.-C.J. Wei, Y.-M. Su, Sputter-deposited 20mol% gadolinia-doped ceria films on 8mol% yttria-stabilized zirconia tapes for improved electrochemical performance, Thin Solid Films. 618 (2016) 202–206. https://doi.org/10.1016/j.tsf.2016.03.009.
[18] Y.-L. Kuo, S.D. Kencana, Mechanism of oxygen ion diffusion in Gd-doped ceria electrolyte films deposited via reactive and direct sputtering, Surf. Coat. Technol. 320 (2017) 47–52. https://doi.org/10.1016/j.surfcoat.2017.02.011.
[19] N. Coppola, P. Polverino, G. Carapella, C. Sacco, A. Galdi, A. Ubaldini, V. Vaiano, D. Montinaro, L. Maritato, C. Pianese, Structural and Electrical Characterization of Sputter-Deposited Gd0.1Ce0.9O2−δ Thin Buffer Layers at the Y-Stabilized Zirconia Electrolyte Interface for IT-Solid Oxide Cells, Catalysts. 8 (2018) 571. https://doi.org/10.3390/catal8120571.
[20] E. Gourba, P. Briois, A. Ringuedé, M. Cassir, A. Billard, Electrical properties of gadolinia-doped ceria thin films deposited by sputtering in view of SOFC application, J. Solid State Electrochem. 8 (2004). https://doi.org/10.1007/s10008-004-0503-3.
[21] P. Briois, A. Billard, A comparison of electrical properties of sputter-deposited electrolyte coatings dedicated to intermediate temperature solid oxide fuel cells, Surf. Coat. Technol. 201 (2006) 1328–1334. https://doi.org/10.1016/j.surfcoat.2006.01.061.
[22] C. Brahim, A. Ringuedé, E. Gourba, M. Cassir, A. Billard, P. Briois, Electrical properties of thin bilayered YSZ/GDC SOFC electrolyte elaborated by sputtering, J. Power Sources. 156 (2006) 45–49. https://doi.org/10.1016/j.jpowsour.2005.08.017.
[23] F.C. Fonseca, S. Uhlenbruck, R. Nedéléc, H.P. Buchkremer, Properties of bias-assisted sputtered gadolinia-doped ceria interlayers for solid oxide fuel cells, J. Power Sources. 195 (2010) 1599–1604. https://doi.org/10.1016/j.jpowsour.2009.09.050.
[24] F.C. Fonseca, S. Uhlenbruck, R. Nédélec, D. Sebold, H.P. Buchkremer, Temperature and Bias Effects on Sputtered Ceria Diffusion Barriers for Solid Oxide Fuel Cells, J. Electrochem. Soc. 157 (2010) B1515–B1519. https://doi.org/10.1149/1.3476296.
[25] T. Klemensø, J. Nielsen, P. Blennow, Å.H. Persson, T. Stegk, B.H. Christensen, S. Sønderby, High performance metal-supported solid oxide fuel cells with Gd-doped ceria barrier layers, J. Power Sources. 196 (2011) 9459–9466. https://doi.org/10.1016/j.jpowsour.2011.07.014.
[26] J. Sakaliūnienė, J. Čyvienė, B. Abakevičienė, J. Dudonis, Investigation of Structural and Optical Properties of GDC Thin Films Deposited by Reactive Magnetron Sputtering, Acta Phys. Pol. A. 120 (2011) 63–65. https://doi.org/10.12693/APhysPolA.120.63.
[27] S. Sønderby, P.L. Popa, J. Lu, B.H. Christensen, K.P. Almtoft, L.P. Nielsen, P. Eklund, Strontium Diffusion in Magnetron Sputtered Gadolinia-Doped Ceria Thin Film Barrier Coatings for Solid Oxide Fuel Cells, Adv. Energy Mater. 3 (2013) 923–929. https://doi.org/10.1002/aenm.201300003.
[28] A.A. Solovyev, A.N. Kovalchuk, I.V. Ionov, S.V. Rabotkin, A.V. Shipilova, D.N. Terentev, Deposition of a Thin-Film CGO Electrolyte for Solid Oxide Fuel Cells, Key Eng. Mater. 685 (2016) 776–780. https://doi.org/10.4028/www.scientific.net/KEM.685.776.
[29] I.V. Ionov, A.A. Solovyev, A.V. Shipilova, A.M. Lebedynskiy, E.A. Smolyanskiy, A.L. Lauk, V.A. Semenov, Reactive co-sputter deposition of nanostructured cermet anodes for solid oxide fuel cells, Jpn. J. Appl. Phys. 57 (2017) 01AF07. https://doi.org/10.7567/JJAP.57.01AF07.

[30] A.A. Solovyev, A.V. Shipilova, I.V. Ionov, A.N. Kovalchuk, S.V. Rabotkin, V.O. Oskirko, Magnetron-Sputtered YSZ and CGO Electrolytes for SOFC, J. Electron. Mater. 45 (2016) 3921–3928. https://doi.org/10.1007/s11664-016-4462-0.
[31] C.H. Londono, L. Combemale, F. Gao, A. Billard, P. Briois, Properties of Gadolinium-doped Ceria (GDC) Films Deposited by Reactive Magnetron Sputtering Processes, ECS Trans. 78 (2017) 1189–1193. https://doi.org/10.1149/07801.1189ecst.
[32] P. Coddet, M.-L. Amany, J. Vulliet, A. Caillard, A.-L. Thomann, YSZ/GDC bilayer and gradient barrier layers deposited by reactive magnetron sputtering for solid oxide cells, Surf. Coat. Technol. 357 (2019) 103–113. https://doi.org/10.1016/j.surfcoat.2018.09.085.
[33] S.V. Rabotkin, V.O. Oskirko, I.V. Ionov, V.A. Semenov, A.V. Shipilova, A.A. Solovyev, Process stabilization during reactive high power impulse magnetron sputtering of Ce/Gd target, J. Phys. Conf. Ser. 1115 (2018) 032078. https://doi.org/10.1088/1742-6596/1115/3/032078.
[34] A.A. Solovyev, S.V. Rabotkin, A.V. Shipilova, I.V. Ionov, Magnetron Sputtering of Gadolinium-doped Ceria Electrolyte for Intermediate Temperature Solid Oxide Fuel Cells, Int. J. Electrochem. Sci. (2019) 575–584. https://doi.org/10.20964/2019.01.03.
[35] L.R. Doolittle, Algorithms for the rapid simulation of Rutherford backscattering spectra, Nucl. Instrum. Methods Phys. Res. Sect. B Beam Interact. Mater. At. 9 (1985) 344–351. https://doi.org/10.1016/0168-583X(85)90762-1.
[36] S. Ershov, M.-E. Druart, M. Poelman, D. Cossement, R. Snyders, M.-G. Olivier, Deposition of cerium oxide thin films by reactive magnetron sputtering for the development of corrosion protective coatings, Corros. Sci. 75 (2013) 158–168. https://doi.org/10.1016/j.corsci.2013.05.028.
[37] S. Van Steenberge, W.P. Leroy, D. Depla, Influence of oxygen flow and film thickness on the texture and microstructure of sputtered ceria thin films, Thin Solid Films. 553 (2014) 2–6. https://doi.org/10.1016/j.tsf.2013.11.049.
[38] H. Windischmann, Intrinsic stress in sputter-deposited thin films, Crit. Rev. Solid State Mater. Sci. 17 (1992) 547–596. https://doi.org/10.1080/10408439208244586.
[39] G. Brauer, H. Gradinger, Über heterotype Mischphasen bei Seltenerdoxyden. I, Z. Für Anorg. Allg. Chem. 276 (1954) 209–226. https://doi.org/10.1002/zaac.19542760502.
[40] M. Wojdyr, Fityk: a general-purpose peak fitting program, J. Appl. Crystallogr. 43 (2010) 1126–1128. https://doi.org/10.1107/S0021889810030499.
[41] C.S. Barrett, T.B. Massalski, Structure of metals: crystallographic methods, principles and data, p. 205, 3rd rev. ed, Pergamon, Oxford ; New York, 1980.
[42] M. Birkholz, P.F. Fewster, C. Genzel, Thin film analysis by X-ray scattering, p. 28, Wiley-VCH, Weinheim, 2006.
[43] T. Schoonjans, A. Brunetti, B. Golosio, M. Sanchez del Rio, V.A. Solé, C. Ferrero, L. Vincze, The xraylib library for X-ray–matter interactions. Recent developments, Spectrochim. Acta Part B At. Spectrosc. 66 (2011) 776–784. https://doi.org/10.1016/j.sab.2011.09.011.
[44] P. Coddet, M.-C. Pera, A. Billard, Planar Solid Oxide Fuel Cell: Electrolyte Deposited by Reactive Magnetron Sputtering and Cell Test, Fuel Cells. 11 (2011) 158–164. https://doi.org/10.1002/fuce.201000123.
[45] P. Briois, C. Mazataud, S. Fourcade, F. Mauvy, J.-C. Grenier, A. Billard, Synthesis and Characterization of Apatite Structure Sputter Deposited Coatings Dedicated to Intermediate Temperature Solid Oxide Fuel Cells, J. Electrochem. Soc. 158 (2011) B1479. https://doi.org/10.1149/2.026112jes.

[46] W. Wu, Z. Zhao, X. Zhang, Z. Liu, D. Cui, B. Tu, D. Ou, M. Cheng, Structure-designed gadolinia doped ceria interlayer for solid oxide fuel cell, Electrochem. Commun. 71 (2016) 43–47. https://doi.org/10.1016/j.elecom.2016.08.005.
[47] J.-M. Zhang, F. Ma, K.-W. Xu, Calculation of the surface energy of FCC metals with modified embedded-atom method, Appl. Surf. Sci. 229 (2004) 34–42. https://doi.org/10.1016/j.apsusc.2003.09.050.
[48] S. Van Steenberge, W.P. Leroy, A. Hubin, D. Depla, Momentum transfer driven textural changes of CeO2 thin films, Appl. Phys. Lett. 105 (2014) 111602. https://doi.org/10.1063/1.4895785.
[49] D.B. Knorr, J.A. Szpunar, Applications of texture in thin films, JOM. 46 (1994) 42–48. https://doi.org/10.1007/BF03222582.

Table I: Fitting parameters of the RBS spectra. The thickness values in parentheses correspond to the thickness of the top layer with an oxygen concentration gradient. The error in the thickness can be estimated to 10×10^{15} atoms/cm².

		As-deposited			**Annealed**		
Distance (cm)	Bias	Thickness (10^{15} atoms/cm²)	Roughness factor (10^{15} atoms/cm²)	x in $Ce_{0.8}Gd_{0.2}O_x$	Thickness (10^{15} atoms/cm²)	Roughness factor (10^{15} atoms/cm²)	x in $Ce_{0.8}Gd_{0.2}O_x$
12.7	Floating	3997 (1400)	206	1.0	5711	322	2
	-40V	3887 (512)	200	1.0	5710	394	2
	-80V	3582 (364)	214	0.9	5802	355	2
16.0	Floating	4335	356	2	4293	402	2
	-40V	4419	300	2	4420	330	2
	-80V	4366	248	2	4406	268	2

Table II: Comparison of power-normalized deposition rates reported in the literature. Transition mode in the sputter regime column means that the authors of the respective publication worked in the unstable transition between the metallic and the oxide mode.

Reference	Type	Sputter regime	Power-normalized deposition rate ($nm\ min^{-1}\ W^{-1}\ cm^2$)
This work	pDC	Metallic mode	15-18
[3]	not reported	not reported	8.0
[46]	not reported	not reported	0.8
[11]	RF	Oxide target	0.3
[12]	RF	Metallic mode	22.1
[16]	RF	Oxide target	0.5
[19]	RF	Oxide target	13.3
[28]	pDC	Transition mode	3.4
[30]	pDC	Transition mode	3.0
[33]	HiPIMS	Transition mode	2.1
[34]	HiPIMS	Transition mode	5.5

Figure caption

Figure 1*: Schematic representation of the deposition chamber, showing the different target-substrate distances as well as the positions of the gas inlet.*

Figure 2*: Typical hysteresis curves for the CeGd target for 2 different pumping speeds. The waiting time between subsequent measurements is 2 minutes in the case of filled symbols and 6 minutes in the case of open symbols. The arrows indicate the direction of increasing or decreasing oxygen flow rate.*

Figure 3*: (a) Hysteresis curve of a Ce/Gd target in an Ar/Oxygen atmosphere. The waiting time between two subsequent measurements is 2 minutes. (b) The time needed to return to the initial voltage after a hysteresis experiment as a function of the time that the target was sputtered in the oxide mode.*

Figure 4*: Evolution of discharge voltage (full symbols) and pressure (open symbols) with the oxygen flow rate for two different target-substrate distances and two different gas inlet positions.*

Figure 5*: RBS spectra of GDC films before and after annealing at 500°C for films deposited at 12.7 cm distance (a,b,c) and films deposited at a 16.0 cm distance (d,e,f) with varying substrate bias (floating, -40 V and – 80 V). The black lines show the simulated spectra that were fitted to the experimental data.*

Figure 6*: X-ray diffractograms of the as-deposited GDC films. The circular markers show the peak positions corresponding to GDC (PDF card 01-075-0162), the square markers correspond to metallic Ce (PDF card 01-071-7442) and the triangles correspond to* Ce_7O_{12} *(PDF card 01-071-0567).*

Figure 7*: X-ray diffractograms of GDC films after annealing at 500°C at short and long distance for various bias voltages in logarithmic scale. The diffractograms are offset by sequential multiplication by a factor of 10.*

Figure 8*: Texture factors of the GDC films after annealing at 500°C at short and long distance for various bias voltages.*

Figure 9*: SEM images of the films before and after the annealing at 500°C*

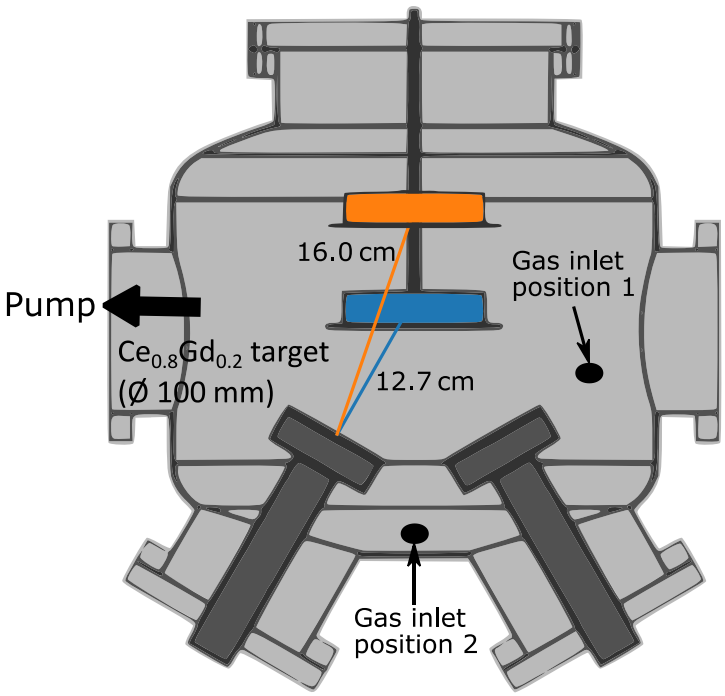
16.0 cm
Gas inlet
position 1
Pump
Ce0.8Gd0.2 target
(Ø 100 mm)
12.7 cm
Gas inlet
position 2

Figure 1

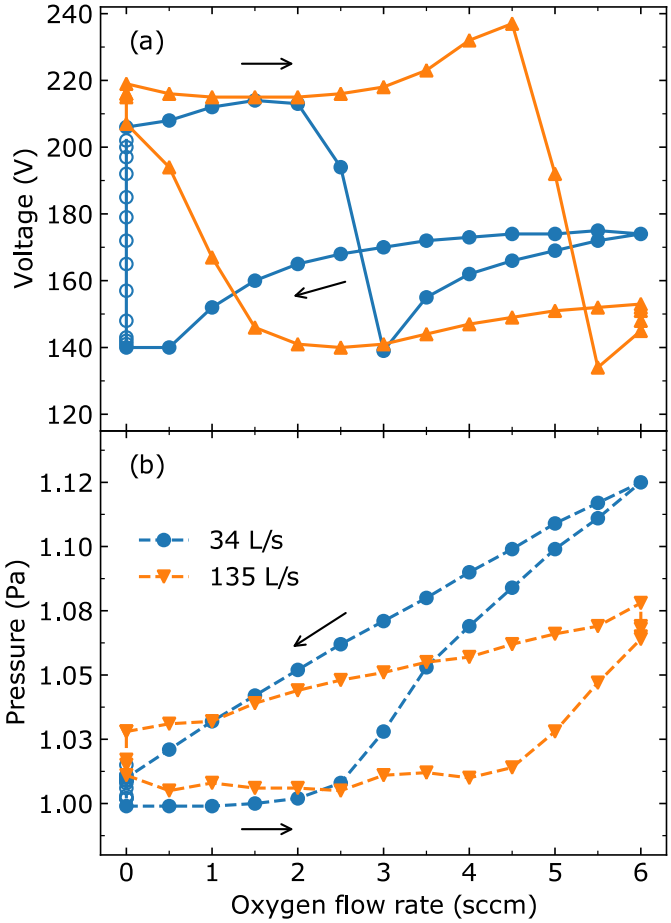
(a)
Voltage (V)
240
220
200
180
160
140
120
(b)
Pressure (Pa)
1.12
1.10
1.08
1.05
1.03
1.00
34 L/s
135 L/s
0
1
2
3
4
5
6
Oxygen flow rate (sccm)

Figure 2

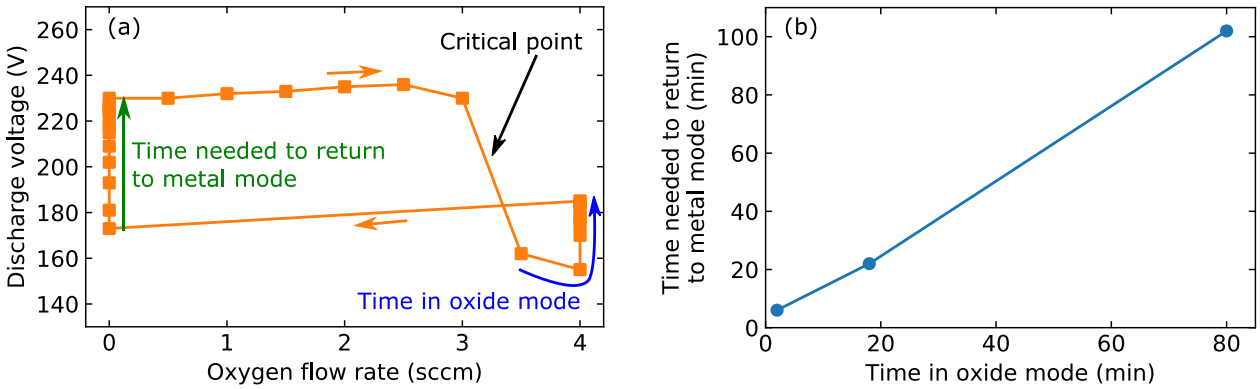
(a)
Critical point
Time needed to return
to metal mode
Time in oxide mode
Discharge voltage (V)
Oxygen flow rate (sccm)
(b)
Time needed to return
to metal mode (min)
Time in oxide mode (min)

Figure 3

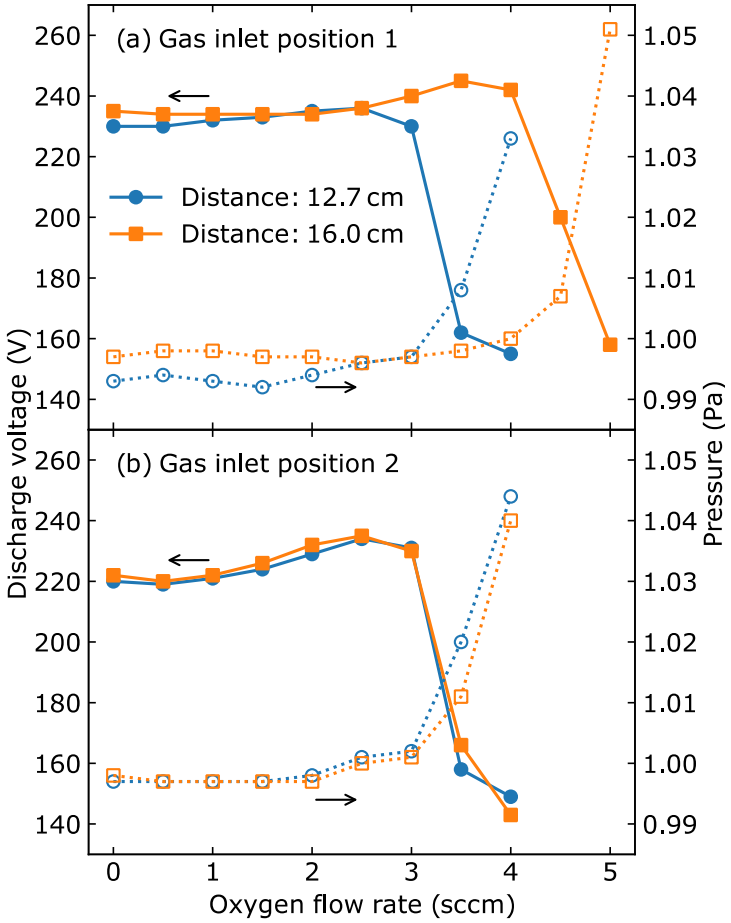
(a) Gas inlet position 1
Distance: 12.7 cm
Distance: 16.0 cm
(b) Gas inlet position 2
Discharge voltage (V)
Pressure (Pa)
Oxygen flow rate (sccm)
260
240
220
200
180
160
140
1.05
1.04
1.03
1.02
1.01
1.00
0.99
0
1
2
3
4
5

Figure 4

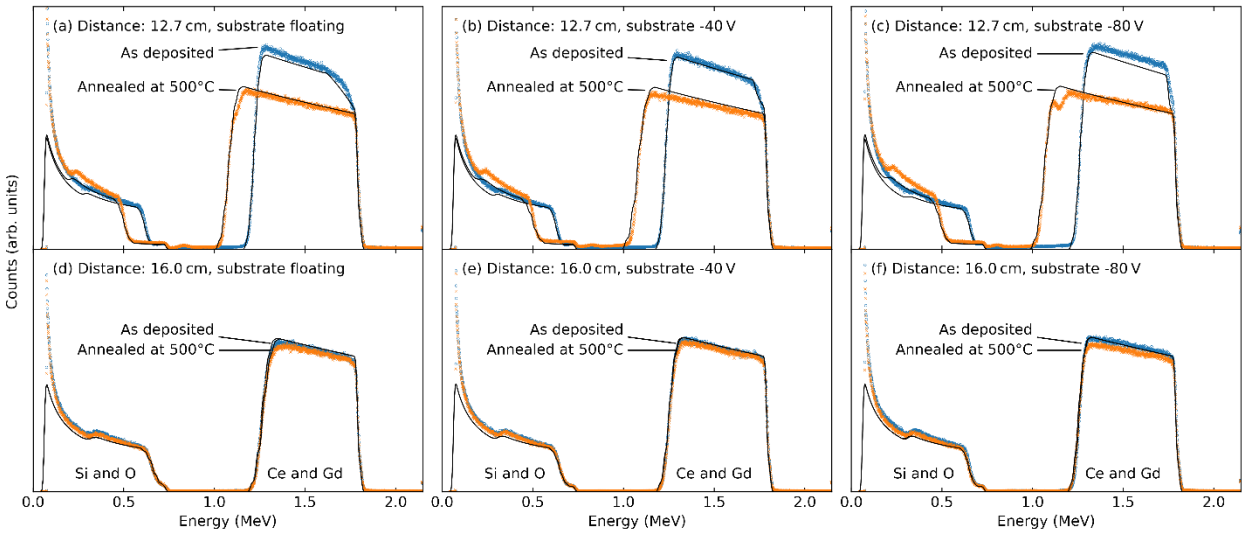
(a) Distance: 12.7 cm, substrate floating
(b) Distance: 12.7 cm, substrate -40 V
(c) Distance: 12.7 cm, substrate -80 V
(d) Distance: 16.0 cm, substrate floating
(e) Distance: 16.0 cm, substrate -40 V
(f) Distance: 16.0 cm, substrate -80 V
As deposited
Annealed at 500°C
Si and O
Ce and Gd
Counts (arb. units)
Energy (MeV)
0.0
0.5
1.0
1.5
2.0

Figure 5

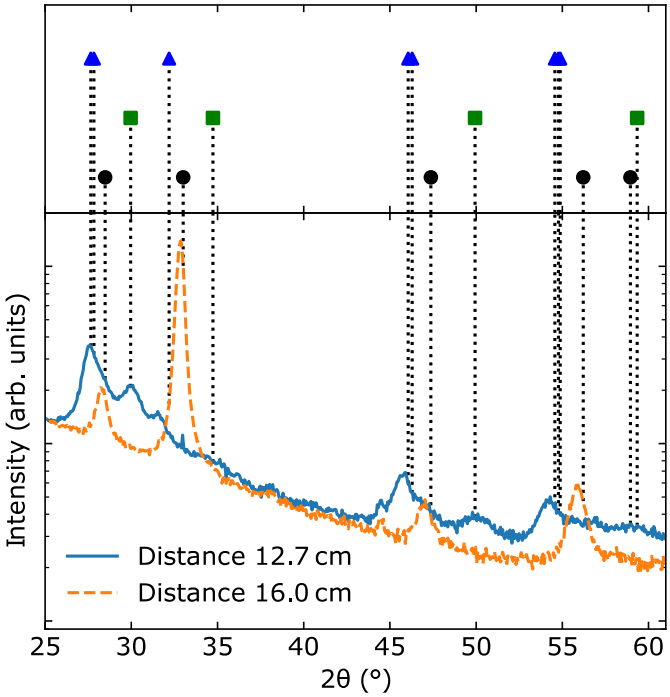
Intensity (arb. units)
Distance 12.7 cm
Distance 16.0 cm
25
30
35
40
45
50
55
60
2θ (°)

Figure 6

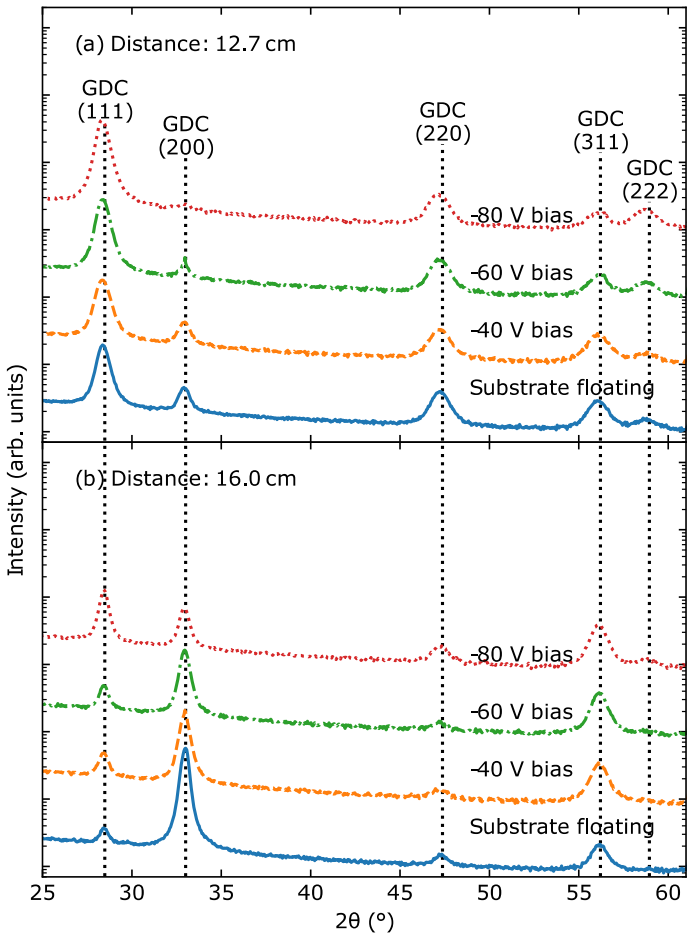
(a) Distance: 12.7 cm
GDC (111)
GDC (200)
GDC (220)
GDC (311)
GDC (222)
-80 V bias
-60 V bias
-40 V bias
Substrate floating
(b) Distance: 16.0 cm
-80 V bias
-60 V bias
-40 V bias
Substrate floating
Intensity (arb. units)
25
30
35
40
45
50
55
60
2θ (°)

Figure 7

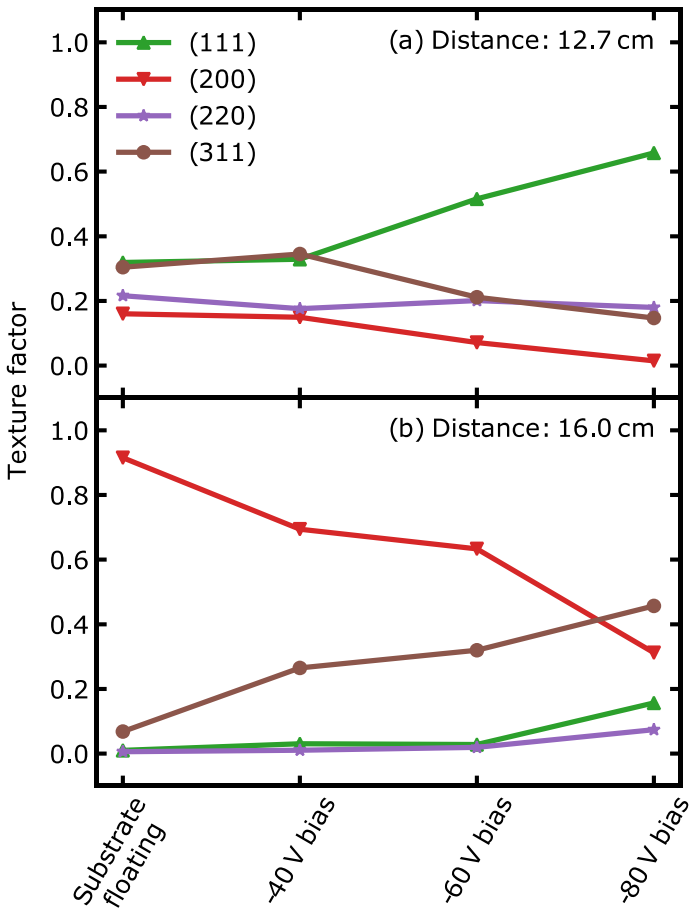
(111)
(200)
(220)
(311)
(a) Distance: 12.7 cm
(b) Distance: 16.0 cm
Texture factor
1.0
0.8
0.6
0.4
0.2
0.0
Substrate floating
-40 V bias
-60 V bias
-80 V bias

Figure 8

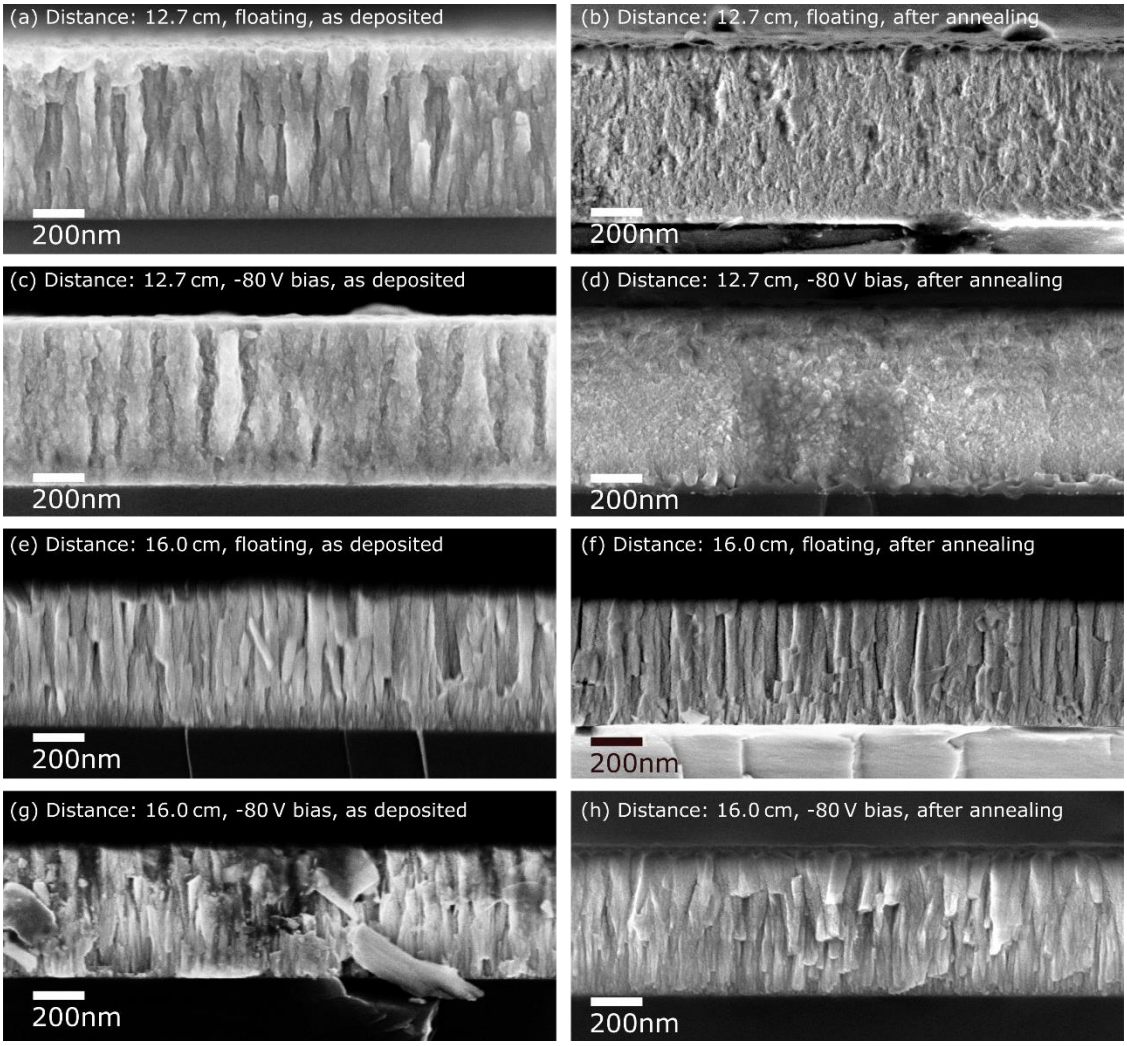
(a) Distance: 12.7 cm, floating, as deposited
200nm
(b) Distance: 12.7 cm, floating, after annealing
200nm
(c) Distance: 12.7 cm, -80 V bias, as deposited
200nm
(d) Distance: 12.7 cm, -80 V bias, after annealing
200nm
(e) Distance: 16.0 cm, floating, as deposited
200nm
(f) Distance: 16.0 cm, floating, after annealing
200nm
(g) Distance: 16.0 cm, -80 V bias, as deposited
200nm
(h) Distance: 16.0 cm, -80 V bias, after annealing
200nm

Figure 9